ORIGINAL ARTICLE

Comparing structural models of linear elastic responses to bending in inosculated joints

Wilfrid Middleton[1] · Halil Ibrahim Erdal[1] · Andreas Detter[2] · Pierluigi D'Acunto[1] · Ferdinand Ludwig[1]

Abstract

Key message **Mechanical models of inosculations benefit from moderate geometric detail and characterisation of the structurally optimised area of interwoven tension-resistant fibres between the branches.**

Abstract Living architecture is formed by shaping and merging trees, often in combination with non-living technical elements. These structures often employ the mechanical and physiological adaptations of living trees to support structural loads. Designed and vernacular buildings utilise inosculations to redistribute forces, redirect growth, and provide redundancy. Mechanical models of inosculations in living architecture must be built according to the adaptations available to the tree. Here, mass allocation and fibre orientation are examined. Under typical gravity loads, a zone at the top of the inosculation is subject to tension. This is of particular interest because a trade-off in fibre orientation between mechanical and physiological optimisation is necessary. In tree forks, this results in specifically adapted interwoven fibres. In this study, Finite Element Analysis (FEA) is used to develop different mechanical models to fit bending experiments of four *Salix alba* inosculations, comparing the models' accuracy in replicating rotations in the joint. Nine models were developed. Three levels of detail of mass allocation are considered for global isotropic (3 models) and orthotropic (3 models) mechanical properties as well as a model including the interwoven tension zone, a model of local branch and trunk orthotropy, and a model combining these two localised features. Results show significant accuracy gains come from moderate geometric accuracy and consideration of the tension-zone optimisation. The construction of the tension zone in FEA is simple and applicable to natural and artificially induced inosculations.

Keywords Living architecture · Inosculation · LiDAR · Finite element analysis · Tree biomechanics · *Salix alba*

Introduction

Inosculations

Inosculation is the process of intergrowth between two or more plant roots, branches or stems. Inosculations provide essential structural support to naturally grown and manipulated trees. Many examples of living architecture, from living root bridges in Meghalaya (India), Sumatra (Indonesia)

and Foshan (China) (Middleton et al. 2020) to the buildings designed with Baubotanik methods in Germany (Ludwig et al. 2019) utilise inosculations. A range of species with diverse benefits (Capuana 2020; McBride 2017) are used in living architecture, including fast-growing species, such as willow, birch, and poplar (Smith 2013; Margaretha 2013; Aliaga 2017; Capuana 2020), and resilient species such as London Plane (Ludwig 2016; Höpfl et al. 2021; McBride 2017). In living architecture, inosculations provide structural support to technical and functional elements, as in the Nagold Plane Tree Cube (Fig. 1a, b) (Ludwig 2012); link the network of elements that create the structural form; or provide path redundancy in water transport, allowing nonfatal failure of individual elements, as shown by living root bridges surviving landslides or cuts by humans (Middleton et al. 2020). In particular, inosculations are a central structural feature of naturally growing strangler figs, many of which are high-value trees in tropical and subtropical cities,

✉ Wilfrid Middleton
  wilfrid.middleton@gmail.com

1 School of Engineering and Design, Technical University of Munich TUM, 80333 Munich, Bavaria, Germany

2 Brudi & Partner TreeConsult and SAG Baumstatik e.V, Gauting, 82131 Bavaria, Germany

Fig. 1 Induced inosculations in *Platanus* x *hispanica*. In the Nagold Plane Tree Cube before inosculation (**a**) and 7 years after inosculation (**b**). A horizontal slice through a pair of inosculated stems of *Plata-nus* x *hispanica* (with the water-conducting xylem dyed pink) – photo produced by Christoph Fleckenstein

such as Mumbai (Linaraki et al. 2021), Hong Kong (Hui et al. 2020) and Singapore (Harrison et al. 2017). In deciduous trees (Slater 2018a), inosculations occur from time to time (6.6% of bifurcations of similar-sized branches surveyed by Slater (2018b) have inosculations) above ground and are common in roots (Graham and Bormann 1966).

Inosculations allow, through their common growth, distribution of both water and mechanical loads between otherwise separate elements. At the inosculation, the living cambium of two or more shoots or roots conjoin and generate a common growth ring (Fig. 1c), as described by Millner (1932). From then on, tissue links the roots and crowns of both trees, allowing the cross-flow of water and nutrients and the reorientation of fibres for mechanical support. Comparing Slater (2018b) and Ludwig (2012), it is clear that the inosculation's mechanical and physiological functions depend on how and when the tissues merge during the inosculation process. This depends largely on the way the constituent trunks are initially joined. As well as providing new pathways for water transport between roots and crowns, the inosculation can perform a structural function—long elements brace one another along their length (Fig. 1a, b), reducing their slenderness ratios and thus the bending stresses. Slater finds that naturally growing trees with inosculations above branch bifurcations invest less in support at the bifurcation (Slater 2018a), indicating the mechanical role of the inosculation in resisting cleavage of the bifurcating branches. In some species, such as *Ficus elastica*, many inosculated aerial roots can form a network with both physiological and mechanical functions, distributing and reducing mechanical

stresses, providing multiple water or nutrient pathways, and building redundancy into the tree. These combined functions underpin the development of Meghalaya's living root bridges (Ludwig et al. 2019) and Baubotanik design (Shu et al. 2021; Middleton et al. 2022; Ludwig 2012; Lievestro 2020). In living architecture, loading regimes are designed according to growth predictions. As the tree grows and elements take form, load distribution can be calculated more precisely. In this iterative process, loading is re-evaluated as the structure grows and is pruned and guided into shape. Numerical models are needed for detailed analysis of inosculations, which change as the structure grows. In contrast to this, in non-grown structures, simple mechanical models inform the broad design and precise numerical models are used in the final stages before construction. Lessons from these models can inform a general understanding of inosculation mechanics, which feeds into future designs.

Mechanical features of inosculations

Typically, mechanical stiffness and strength in tree joint optimisation come from two macroscopic features: mass growth and fibre orientation. By adding mass, the tree distributes stresses over a wider area. Mattheck describes the uniform stress hypothesis in which trees can allocate mass to reduce stress gradients, thereby efficiently avoiding potentially dangerous stress concentrations. For more details, compare Mattheck and Bethge (1998) and Slater (2021). The fibre orientation defines the direction of relative strength and stiffness of the wood and the direction of water transport. Across a range of species, Young's modulus parallel to the

fibres of clear dry wood is around 10–30 times higher than across it within the growth ring (the tangential direction); and compressive strength is typically 6 to 13 times larger parallel to the fibres than perpendicular to it, for the same species (Kretschmann 2010).

These sources can simultaneously contribute to mechanical optimisation, particularly in branch junctions (Müller et al. 2006), where stresses are high and where adaptations serve to level out longitudinal fibre deformations, resulting in constant strains instead of constant stresses. Some authors have investigated specific optimisations at branch junctions (Pfisterer and Spatz 2008; Haushahn et al. 2014; Beismann et al. 2000) or the specific fracture strength of branch junctions (Farrell 2003; Gilman 2003; Kane 2007) whilst others provide a general understanding of structural attachment (Shigo 1985).

Of naturally occurring branch junctions, inosculated branch or stem pairs of similar size, like those designed in Baubotanik (Fig. 1), mostly resemble tree forks. As described by many authors (Slater and Ennos 2013, Wessolly and Erb 2014, Pfisterer and Spatz 2008), a fork typically resists compressive forces in the outer edge of each branch and, more importantly, tensile forces in the middle section between the two branches. In Baubotanik-designed inosculations, elements growing at diagonals and supporting dead and live loads (Fig. 1a, b) create tension forces in the inosculation between the branches. Throughout this study, in analogy to forked trees, the parts of the tree pairs above an inosculation (leading to the canopy) are called branches whilst those below the inosculation (leading to the roots) are called trunks. After the formation of a common growth ring, the top side of an inosculation can be seen as similar to a tree fork: two branches rising from a common joint (Ludwig 2012). As described in Slater et al. (2014), the wood fibre in forks must combine mechanical function (Fig. 2a) with the physiological function of water transport from roots to stem (Fig. 2b). These functions converge in the compressive area, with forces running along the fork from base to top. In the tension area, the forces run from branch to branch, which is not a viable water transport path. Slater et al. (2014) anatomical investigations show that in this tension zone, fibres passing from the upper side of the branch down to the stem interweave (Fig. 2c, d). This provides a pathway for water transport whilst allowing transmission of forces along the fibres, stretching instead of cleaving them. This is a combination of mass addition and fibre orientation.

A mechanical model of inosculations

A mechanical model of inosculations should include realistic material characterisation, be geometrically precise, and involve a construction that reflects the basic features of fibre orientation optimisation.
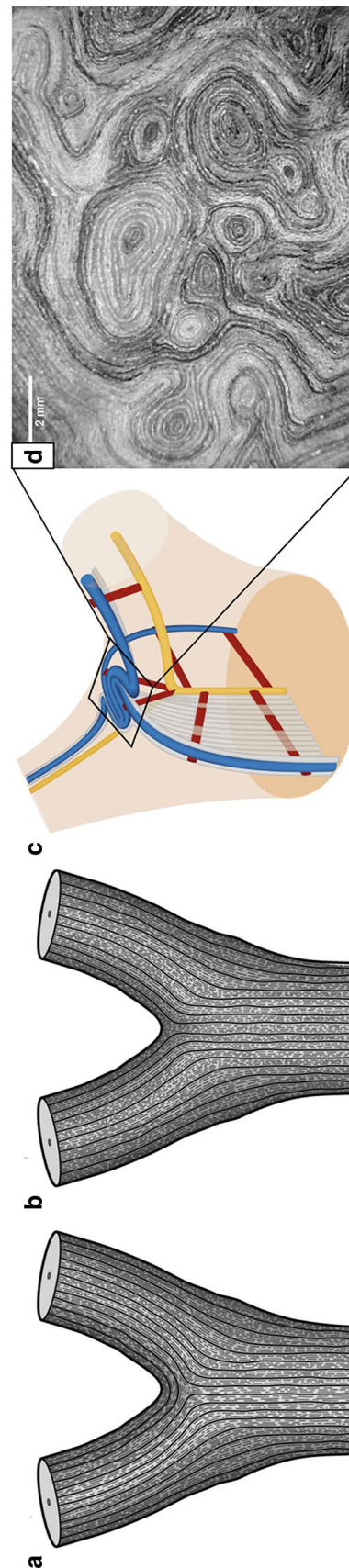

Fig. 2 From Slater et al (2014): a fork with idealised fibril orientation for tension-zone mechanics (**a**) and for water transport from branches to roots (**b**). A model of the tension zone (interwoven vessels in blue, piths in blue, fibres in yellow, fibres in white and rays in red), compromising mechanics and water transport (**c**). Interwoven fibres are visible by simply debarking a fork of common ash—(**d**) shows the interwoven zone, photographed from above

Over the last few years, the 3D-capture of complex shapes and representation of them in mechanical models has made significant progress. Recent improvements in cameras and LiDAR scanners have increased capacity for precise documentation (Middleton et al. 2019; Jackson et al. 2019). The resulting point clouds allow detailed maps of tree geometry, previously typically modelled as cylinders informed by diameters at key points. Software for comparing and manipulating point clouds is widely available. Steps have been made in utilising the detail provided by the resulting point clouds (Middleton et al. 2022). Photogrammetry is now affordable to many, whilst the cost of the most precise LiDAR scanners remains high. Additionally, constructing suitable meshes for FEA is still a time-consuming task that is generally not yet automated. Designers must find a balance between geometric detail and resource investment.

Recent detailed structural studies of trees recommend the use of orthotropic properties in the future research (Jackson et al. 2019; Burcham 2020). Whilst Young's modulus in clear, straight-grained green timber is generally well mechanically characterised along the fibre (Niklas and Spatz 2010), the equivalent data are generally missing in the across-fibre directions and in wood with abnormalities or natural optimisations for branching (Davies et al. 2016; Ozyhar et al. 2013; Dounar et al. 2020). As a result, mechanical models of living trees rarely include orthotropic mechanical properties. Vojackova models orthotropy in a single branch (Vojáčková et al. 2019), though other studies avoid orthotropy due to the paucity of material property data (Moravčík et al. 2021; Jackson et al. 2019; Yang et al. 2014; Burcham 2020).

The aim of this study is to develop a model for the mechanical behaviour of inosculations in the elastic range that adequately includes geometry, material properties and fibre orientation. Therefore, the central research question is: what are the relative benefits of including geometric detail and orthotropic material optimisations in mechanical models that can be used during living architecture's iterative process of design and maintenance? The models should be simple enough to be applied to diverse inosculations and should result in a deeper understanding of the key mechanical optimisations at play in inosculations.

In this paper, different model features are compared to understand their relative contributions to an inosculation's mechanical behaviour by replicating an experimental bending test in finite element analysis (FEA). Firstly, isotropic and orthotropic material properties are compared. Then, three levels of geometric detail are compared. Finally, a model of the tension zone suggested by Slater is compared with a model of local elemental orthotropy, a combination of these two, and the global isotropic and orthotropic models. In addition, we present qualitative results of bending tests

beyond the elastic limits to stimulate future research on the failure modes of inosculations.

Methods

Bending tests

Four pairs of white willow *Salix alba* trees (labelled and referred to herein as A12, A14, A24 and B13) at 14 years of age were chosen from a field of 62 inosculated tree pairs to conduct force measurements under bending in May 2021. The four pairs were selected for the clear alignment of the bases of the two trunks, inosculation (also referred to herein as the 'joint'), and branches in a single plane so that the out-of-plane bending caused by pulling would be limited. In A12, the trunk widths differed significantly and the smaller branch was pulled. In A14, A24, and B13, the branch with a suitable attachment point for the pulling cable that was best aligned with the bending plane was chosen for winching. This also determined the position of the force point on the branch, which was 27 cm, 30 cm, 35 cm and 56 cm from the top of the inosculation in B13, B24, A12 and A14 respectively. Each tree was pulled with a 7.8 kN winch from an anchor point 3–10 m away, connected to the tree by a forcemeter. The winch position was chosen to allow a close to 90° angle between the force direction and the pulled branch, maximising the component of the force that acts in bending and minimising unwanted axial forces along the branch. The tree pairs were bent with steadily increasing force and released six times within the elastic range. Several days later, each tree was then pulled a seventh time to failure, ignoring these limits.

Standalone biaxial inclinometers and triaxial inclinometers (built into elastometers) were used to measure the rotation of the tree pair at several points, as shown in Fig. 3. Additionally, non-inclinometric elastometers were used during the six pulling experiments within the elastic range, to ensure the elastic limit was not reached: no more than 0.1% strain was allowed in any elastometer (Wessolly and Erb 2014). No more than 0.20° of rotation was allowed at the base, a limit for damage to the root base (Detter et al. 2013). Apart from this gauge of maximum strain in the pulling experiments below the elastic limit, the elastometric data are not used in the present study. All devices were standard TreeQinetic devices, run with the PiCUS TreeQinetic software (Argus-Electronic 2016).

Different setups were used in the initial six pulls and the seventh pull. In the first six pulls, four biaxial inclinometers and two triaxial inclinometers were used. Biaxial inclinometers were placed below the force point (yellow arrows in Fig. 3) and above and below the inosculation for all six pulls, and at the back and front foot for three pulls
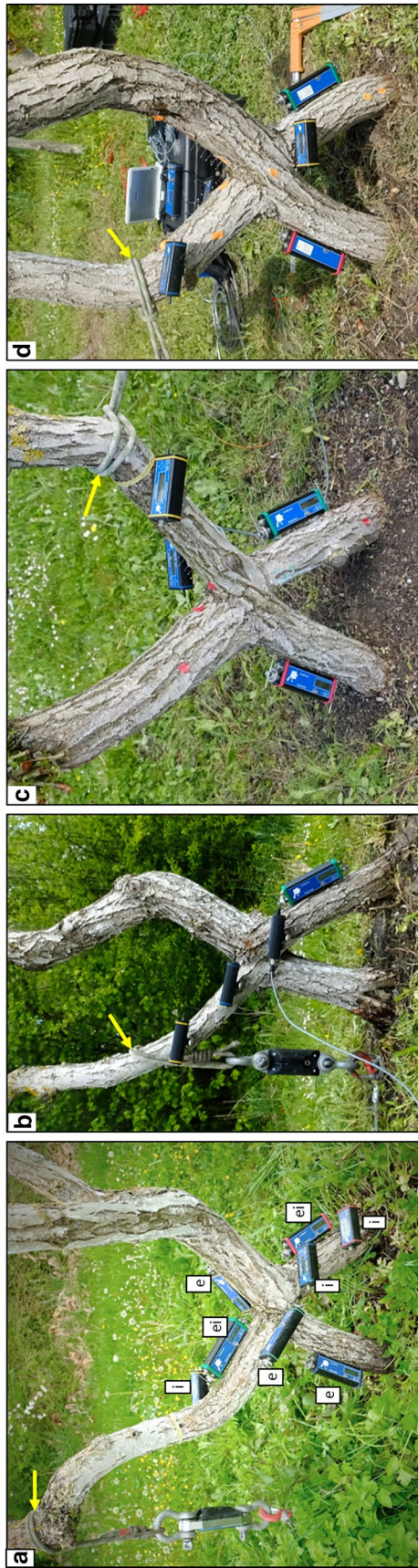
Fig. 3 Tree pairs A14, A12, A24 and B13 in (**a**), (**b**), (**c**) and (**d**) respectively, with measurement devices. Labelled in (**a**) inclinometers, i, and elastometers with in-built inclinometers, ei, provide the rotation data used in this study. Elastometers, e in (**a**), ensure the elastic limits of the trees are not reached. Yellow arrows mark each force point

each. Triaxial inclinometers were placed on the back leg and the pulled branch, providing seven rotation measurement points in total. Additionally, three standalone elastometers without built-in inclinometers were placed around the tree pair (labelled 'e' in Fig. 3a) to check elastic limits were not exceeded. In the seventh pull, three biaxial inclinometers (below the force point, above and below the inosculation) and two triaxial inclinometers (one on each leg) were used — totalling five rotation measurement points (no standalone elastometers were used). All instruments were aligned to the bending plane. Whilst the biaxial inclinometers measure in-plane and out-of-plane rotations separately (allowing direct comparison with in-plane rotation in the FEA model), the triaxial inclinometers do not separate these rotations, but provide a resultant value of the vector sum of the three directions they measure.

Material characterisation

Orthotropic material properties of *S. alba* wood are sparsely documented. Some databases provide isotropic stiffness and strength data (Meier 2022; Matweb 2022), whilst several studies, some of which are summarised by Leclercq (1997), describe dry orthotropic strength properties. No study of orthotropic green *S. alba* properties was found. Van Casteren et al. (2012) find the Young's modulus of green *S. alba* branches to be around 5 GPa, Kretschmann's detailed catalogue of the mechanical properties of green and dry wood includes species similar to *S. alba*: yellow poplar and black willow (Kretschmann 2010). Leclercq describes several mechanical properties of dry *S. alba* wood (such as compressive strength) along and perpendicular to the fibre (i.e. not differentiating between radial and tangential directions), five of which are also presented by Kretschmann (2010) for dry wood of 30 other species. Considering the relationship between green and dry wood, few studies have been made that compare orthotropic mechanical properties (Davies et al. 2016; Liu et al. 2019), and none that considers *S. alba* or similar species. Only the Young's modulus measured along the fibre direction (E_L) is well documented in green and dry wood—it is catalogued for 30 species (not including *S. alba*) by Kretschmann (2010). From this data, it can be seen that $E_{L,dry}$ is a good indicator of $E_{L,green}$: a linear regression of $E_{L,green} = 0.73*E_{L,dry} + 775$ MPa has an R^2 value of 0.915. Whilst Kretschmann (2010) notes an increase in stiffness properties with a decrease in moisture content, few other relevant data are available.

This study draws primarily on two sources: Kretschmann's (2010) orthotropic properties for dry wood of 30 species (not including *S. alba*); and the five aforementioned mechanical properties in Leclercq's (1997) study of *S. alba* and the corresponding properties in Kretschmann's (2010) catalogue of 30 other species. These five properties and Leclercq's (1997)

values for *S. alba* are shown in Table 1, in columns 1 and 2 respectively. To derive orthotropic mechanical properties of green *S. alba* wood from literature data, this study follows four steps (shown in Fig. 4).

In the first step, a linear regression between each of the properties in column 1 of Table 1 (e.g. shear strength, τ) and each of the dry orthotropic properties (e.g. radial Young's modulus E_R) is found for the 30 species in Kretschmann's (2010) dataset (for example, $E_R = 0.119*\tau + 110$). The R^2 regression coefficient is noted in each case (for the given example, $R^2_{ER,\tau} = 0.572$). Five regressions inform each of the nine dry orthotropic properties.

In the second step, Leclercq's (1997) values for *S. alba* (the values in column 2 of Table 1) are fed into these regressions, predicting the orthotropic properties of dry *S. alba*. For the given example, $E_R = 119*6.31 + 110 = 861$ MPa (columns 3–5, Table 1). A weighted mean of the five linear regressions informs each of the nine dry orthotropic properties. The weights (column 7 of Table 1) are proportionate to the regression coefficients (column 6 of Table 1), with the contributions (column 8 of Table 1) summing to produce properties for dry orthotropic *S. alba*. Table 1 shows this calculation for E_R (the final column sums to 919 MPa).

In the third step, due to the paucity of data on *S. alba* green wood, four candidate sets of orthotropic properties are compared for replication of the experimental results for tree pair A14. One of these sets is then taken forward as the 'green' *S. alba* properties. The sets are: set 1, the 'dry' properties calculated above; set 2, the dry properties calculated above, with E_L modified by the linear regression between $E_{L,green}$ and $E_{L,dry}$ stated in the opening paragraph of this section; set 3, the modification in set 2 applied to all Young's moduli and shear moduli, not only to E_L; and set 4, using the properties of set 2 with all other properties (other than E_L) modified by the ratios to E_L described by Davies et al (2016) for Monterey pine. Each set was compared with the experimental data from tree pair A14, in the 'Slater' and 'isotropic' models (described in "Structural model configurations"), on P5 meshes (described in "Geometric detail"). Sets 1, 2 and 3 were similarly accurate ($R^2 = 0.67$, 0.66 and 0.64 respectively) and better than set 4 ($R^2 = 0.56$) in the Slater model. In the isotropic model, all four sets were similar ($R^2 = 0.375$, 0.371, 0.367, and 0.371, respectively). Given the similar accuracy of sets 1, 2 and 3, the relative accuracy ($R^2 = 0.915$) of the linear regression between green and dry wood ($E_{L,green} = 0.73*E_{L,dry} + 775$ MPa), and the lack of data for other green-dry property relations, property set 2 was used. This results in a significant assumption that the differences between green and dry wood in each property apart from E_L are negligible. This may limit the accuracy of the models.

Finally, the radial and tangential directions are simplified into one direction 'perpendicular to the fibre' due to the convoluted growth rings within the joint (see Fig. 2d). The

Table 1 Calculation of E_R using weighted linear regressions, derived from Kretschmann (2010) and fed with Leclercq's (1997) properties for *S. alba*

Property	Leclercq (1997), LQ	For E_R					
		m	C	$E_{R,LQ} = m*LQ+C$	R^2	R^2 weighting ($R^2_{LQ} \div \sum R^2$)	$E_{R,LQ}$ contribution
Specific gravity	0.382	2474	49	995	0.393	0.243	242
Young's modulus parallel to fibre, E_L	5290 MPa	0.0748	393	794	0.139	0.086	68
Shear strength, τ	6.31 MPa	119	110	861	0.572	0.353	304
Compressive strength parallel to fibre, $\sigma_{c,L}$	27 MPa	0.0204	326	875	0.212	0.131	115
Tensile strength perpendicular to fibre, $\sigma_{t,\perp}$	2.145 MPa	0.161	67	1017	0.303	0.187	190

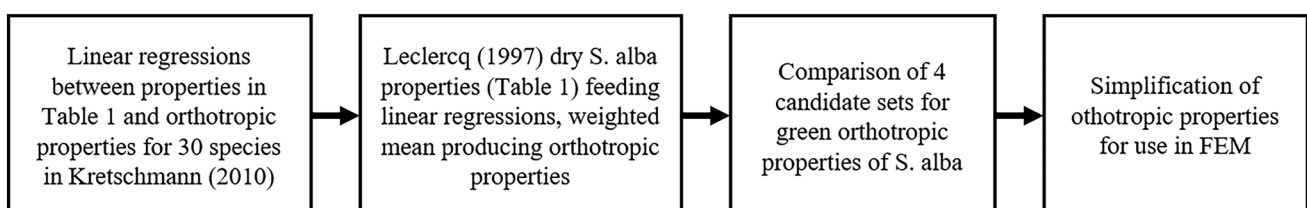| Linear regressions between properties in Table 1 and orthotropic properties for 30 species in Kretschmann (2010) | → | Leclercq (1997) dry *S. alba* properties (Table 1) feeding linear regressions, weighted mean producing orthotropic properties | → | Comparison of 4 candidate sets for green orthotropic properties of *S. alba* | → | Simplification of othotropic properties for use in FEM |

Fig. 4 Flow chart of derivation of orthotropic material properties of green *S. alba* wood

growth rings, and the radial and tangential directions along and across them, are unclear without destructive microscopy. Therefore, from the derived orthotropic values, a mean of the tangential and radial directions is taken as the perpendicular direction to the fibre orientation, resulting in simplified orthotropic properties. In the finite element models, these are compared with isotropic properties (see Table 2). In line with previous studies (Jackson et al. 2019; Moravčík et al. 2021), the longitudinal Young's modulus and shear modulus are applied in isotropy, whilst the Poisson's ratio used is the mean of the two Poisson's ratios derived from longitudinal pressure (resulting in radial deformation, υ_{lr}; and resulting in tangential deformation, υ_{lt}).

Geometric detail

Three levels of geometric detail are compared: a cylinder model and two Poisson surface meshes. A simple cylinder model that replicates a basic tree mechanical model and the typical level of detail used in growth prediction models (element length and radius). A LiDAR point cloud is used to generate Poisson surface meshes at two levels of detail. This is performed in CloudCompare (v2.11.3) (Girardeau-Montaut 2011), which uses an octree to determine relative precision. An octree divides the model volume into 8 sub-volumes with each increasing level of 'depth'. A mesh of octree depth 5 ('P5' mesh) is a relatively precise reconstruction that requires minimal work in preparing the mesh for analysis. A mesh of octree depth 6 ('P6' mesh) requires significant mesh preparation and has a higher level of precision. The average distance between the mesh and the LiDAR point cloud is 21 mm, 2.7 mm and 1.7 mm in the cylinder, P5 and P6 models respectively. All LiDAR point clouds were generated from two to four scans of the trees with a Riegl LMS-Z420i at 3-4 m scan distance. Kersten et al. (2009) find the LMS-z420i has 2-4 mm accuracy at up to 205 m distance to the target. A 5 mm voxel point cloud was produced using RiSCAN Pro (Riegl 2010).

Structural model configurations

The meshes were pre-processed in Meshlab (Cignoni 2018), creating closed-surface 2D meshes with triangular elements. They were then imported into SpaceClaim (Ansys 2022b), where they were converted to tetrahedral volumetric meshes.

The cylindrical meshes consist of around 30,000 elements, whilst the P5 and P6 meshes consist of 10,000–15,000 and 40,000–45,000 elements, respectively. Ansys Mechanical (Ansys 2022a) was used for static finite element analysis.

The material properties were applied to the P5 mesh in five different model configurations, shown in Fig. 5. The first configuration is an isotropic material (Fig. 5a). The second (Fig. 5b) is an orthotropic material applied with a global orientation (the fibres running vertically from the ground to the top of the model). The third (Fig. 5c) is a local element orthotropic model with four parts (one for each branch and trunk), segmenting the joint into four. The fourth is a global orthotropic model (as in the second) with the upper middle part of the joint oriented so the fibres are in the plane of bending, reflecting Slater's proposal of this area utilising the fibres' longitudinal stiffness (Fig. 5d). The fifth combines the local orthotropy of the third configuration and the middle section proposed by Slater (Fig. 5e). To compare isotropic and global orthotropic models, the first (Fig. 5a) and second (Fig. 5b) configurations were applied to the cylindrical (2 models) and P6 models (2 models), as well as the aforementioned P5 models. Table 3 lists the models and the comparison groups.

In each model, winching loads were applied to a node corresponding to the force points marked in Fig. 3, in the direction of the winch, guided by the LiDAR point cloud. As the core experiments were of elastic range bending, all model parts only used elastic material properties. All model constituent parts (e.g. the five parts shown in Fig. 5e) were connected at nodes, such that no displacement could occur between the nodes in each part. Characterising complex soil-root interactions is a major field of study (Yang et al. 2017). In the present finite element model, a range of soil stiffness modulus values (between 0.005N/mm^3 and 2N/mm^3) were tested. A rotation spring stiffness of 1N/mm^3, applied to all underground faces, was found to replicate the trunk base rotations most effectively and was used in all models. This meant no displacements or rotations were fixed at any point as boundary conditions. Whilst this is significantly higher than typical soil stiffness values (Bowles 1988), it accounts for the otherwise unknown root system stiffness.

Each inclinometer is attached to the tree at two points of contact. Corresponding points were located in the FEA-generated meshes. A line was drawn between these points in the models. The in-plane rotations of the FEA model at these points were compared with the in-plane rotations measured by the inclinometers in the field. The quality of fit

Table 2 Inferred isotropic and orthotropic mechanical properties for green *S. alba* used in the finite element analysis

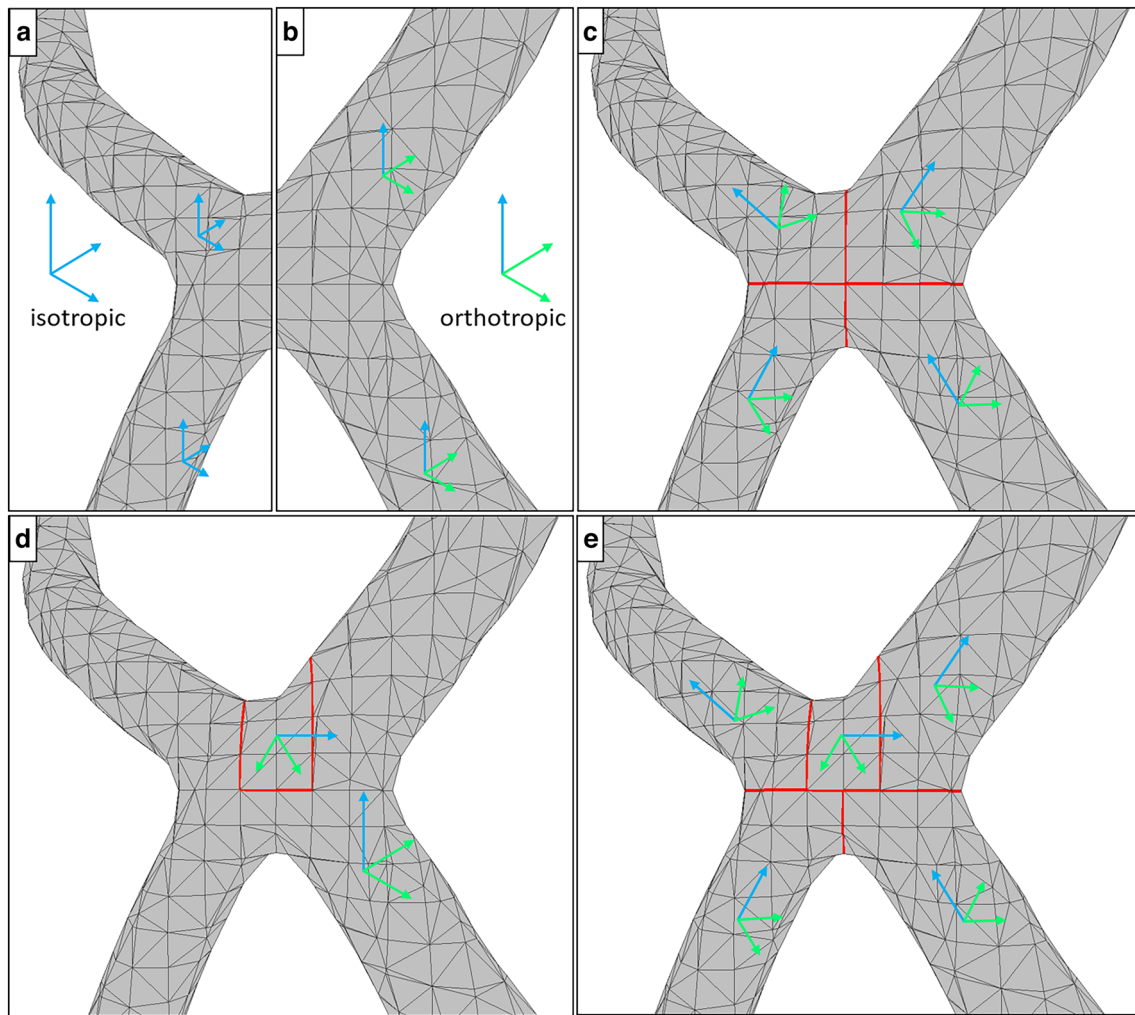|	Specific gravity ρ	Young's modulus E_L, MPa	Young's modulus $E_{R,T}$, MPa	Shear modulus $G_{LR,LT}$, MPa	Shear modulus G_{RT}, MPa	Poisson ratio $\upsilon_{LR,LT}$	Poisson ratio υ_{RT}
Isotropic	0.357	4639	4639	426	426	0.355	0.355
Orthotropic	0.357	4639	715	426	9.26	0.348	0.361

Fig. 5 The P5 Poisson mesh of A14 split into parts for the five model configurations: the isotropic (**a**) and orthotropic (**b**) global models, the elemental orthotropic model (**c**), the Slater model (**d**), and the combined model (**e**). **a** and **b** are also constructed in P6 and cylindrical models, totalling 9 models

Table 3 All nine models built for each tree pair and the three lines of comparison relevant to each. 'Iso' and 'ortho' stand for isotropic and orthotropic, respectively

Model	Isotropic cylinder	Orthotropic cylinder	Iso P5	Ortho P5	Iso P6	Ortho P6	Elemental ortho P5	Slater P5	Combined P5
Isotropy vs orthotropy	✓	✓	✓	✓	✓	✓			
Geometric detail	✓	✓	✓	✓	✓	✓			
Localised features (P5)			✓	✓			✓	✓	✓

of the rotations in each model to the experimental data was assessed by R^2 values.

Results

R^2 values are used as a measure of accuracy throughout. As these differ between measurement points, to compare them (between geometric detail, material characterisation, or structural models), they are normalised to the mean

of R^2 values considered at each measurement point. All results described below refer to the in-plane rotations as measured by the inclinometers, compared between the FEA models and experimental results.

Each tree pair reached its elastic limit at a different load. In A12, A14 and A24, the elastic range limit (0.1% strain) was reached in the pulled branch at 0.1kN, 0.2kN and 0.6kN respectively. In B13, the elastic limit was reached at the base (0.20° of rotation) at 1.4 kN. Failure occurred first in the pulled branch in trees A12 and A14, in the tension zone of the joint in A24 (in the tension zone) and by base-overturning in B13. Photographs of each tree pair before testing and after failure are shown in Supplementary Material A.

The models captured the behaviour of A14, A24 and B13 (average $R^2 = 0.53$ across all models) better than A12 ($R^2 = 0.38$). Within each tree pair, model accuracy varies significantly between measurement points, pointing to the significance of localised mechanical features. As the models compared in this study are of the inosculation mechanics, the results around the inosculation are compared below. Graphs of experimental data and models for each measurement point of each tree are in Supplementary Material B. Rotations in the biaxial inclinometers were predominantly in-plane, and average out-of-plane rotation in the inclinometer nearest the force point is 20% of the in-plane rotation. Out-of-plane rotations are higher near to the force point. Near the ground,

both in-plane and out-of-plane rotations are considerably smaller and more impacted by random error, reflected by larger out-of-plane rotations relative to in-plane rotations.

Material characterisation

Isotropic and orthotropic models were compared. Each group includes 24 measurement points (four tree pairs at three geometric detail levels, above and below the joint). At 15 of 24 points, the orthotropic models are more accurate. As shown in Fig. 6a, the orthotropic models have a higher median accuracy and higher interquartile values than the isotropic models. The cylindrical models were mostly unaffected by orthotropic characterisation (R^2 increased on average by 0.026) whilst the P5 and P6 were more affected (R^2 increased on average 0.071 and 0.070 respectively). Figure 7 shows the models and data for A14, below (7a) and above (7b) the inosculation (also in in Supplementary Material B). The orthotropic Poisson mesh models generally predict more rotation (i.e. less stiffness) than occurred in the experiment, whilst the isotropic and all cylindrical models generally predicted higher stiffness than the real tree.
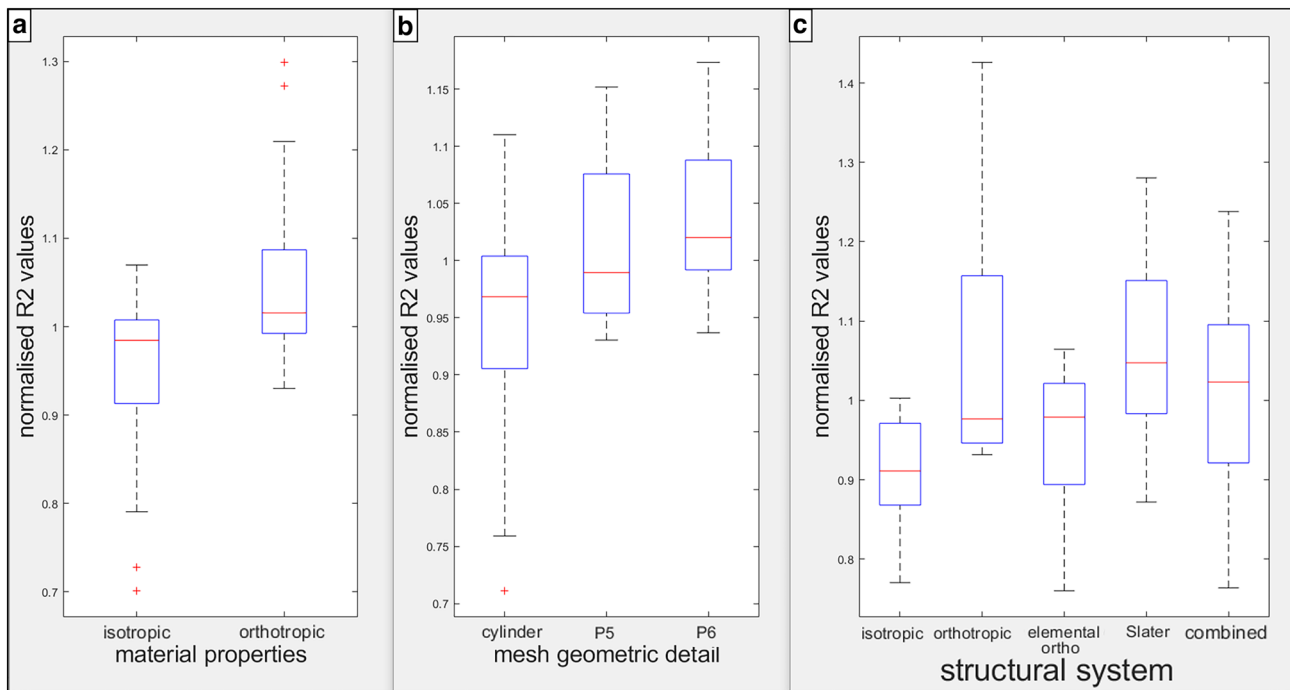

Fig. 6 Model R^2 values (normalised to the measurement point mean) in predicting in-plane rotation above and below the joint: in isotropic and global orthotropic material characterisations (**a**) at three levels of geometric detail (**b**) and five structural model configurations applied to a P5 mesh (**c**)
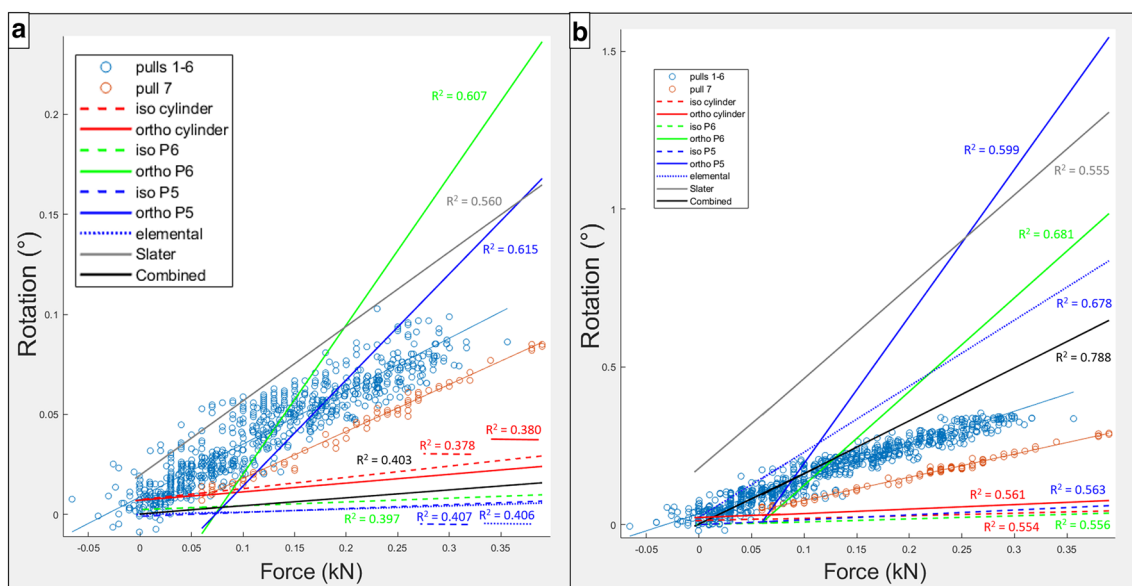
Fig. 7 Experimental and model data below (**a**) and above (**b**) the inosculation in A14

Geometric detail

Geometric detail is compared for isotropic and (global) orthotropic models above and below the joint in four tree pairs (totalling 16 measurement points). The P5 mesh models are more accurate than the cylinder models at 11 of 16 points. The P6 mesh is more accurate than the P5 mesh at 6 of 16 points. As shown in Fig. 6b, the median normalised P6 R^2 value is slightly higher than the P5 median and significantly higher than the cylinder model median.

Structural model configurations

The five structural model configurations (Fig. 5) are compared in a P5 mesh, above and below the inosculation for all four tree pairs (totalling 8 measurement points). The isotropic model is the least accurate, followed by the global and elemental orthotropic models respectively. The Slater model is the most accurate, followed by the combined model. As shown in Fig. 6c, there is significant variation within structural models, particularly in the orthotropic model. R^2 values vary between tree pairs: A12 R^2 values range from 0.279 to 0.463, whilst R^2 ranges from 0.403 to 0.788 in A14.

Discussion

This study finds that improvements in elastic model accuracy arise from both higher geometric precision and detailed structural models (based on changes in the representation of localised fibre direction), independently and in combination with one another. Whilst the improvements in cylindrical models caused by moving from isotropic to orthotropic materials are small, the equivalent improvements in the Poisson meshes are larger. The P6 models are not consistently more accurate than the P5 models. This points to the benefits of combining moderate geometric detail and orthotropic material property characterisation. Whilst the local orthotropic model was an improvement over the isotropic model, it was not as accurate as the (less complicated) global orthotropic model. In contrast, the Slater-style tension zone significantly improves accuracy. This leads to the key result of the study: that, more than high geometric detail or precise material characterisation, the correct identification of specific optimisations should inform living architecture mechanics models. Documenting and meshing highly detailed geometry can be expensive and time-consuming with diminishing marginal returns in accuracy, compared with the benefits of moderate geometric detail and meshes that characterise mechanical optimisations such as Slater's tension zone.

In the iterative design process, the required level of geometric detail can come from two sources; direct documentation and growth prediction. Direct documentation can come from periodic photogrammetric or LiDAR surveys. Two directions for application of the present findings are recommended. First, studies building predictive models of inosculation mass growth (combined with pruning plans, based on initial and environmental conditions) can incorporate the changing mechanics of the inosculation. Second, visual methods for assessing inosculations for mechanical strengths/defects can be developed that consider the Slater tension zone, incorporating the present study's

findings into growth design and guidance practice without the need for detailed numerical models.

Further development of the models presented here should reflect the developmental features common to a broad range of inosculations. A sister study to this one (in review) compares the structure of inosculations with tree forks, describing similar mechanical-physiological trade-offs. Anatomical investigations would provide the botanical perspective related to the present mechanical investigations. Improved orthotropic mechanical characterisation of green wood is needed in most species, including *S. alba*. This includes characterisation of wood in the inosculation, and specifically tension wood in hardwood species. This would shed light on the relevance of the material properties used (and the underpinning assumptions relating the properties of dry and green wood). This would allow application of a range of mechanical properties to the models, testing for accuracy in replicating the experimental results. Characterisation of inelastic behaviour may shed light on the failure modes presented here, which remain a point of interest and not a key result of this study (given the limited number of failure mode data points). The basic level of geometric precision achieved by the P5 meshes requires neither high computation nor human time investment whilst the P6 meshes require significantly more human hours to prepare. More detailed meshes demand more computation time. When utilising these techniques, practitioners must find a balance between mechanical precision and time input. Mesh precision also informs the necessary documentation precision, with photogrammetry, mobile LiDAR and terrestrial LiDAR offering different levels of detail.

The Slater-style tension zone may be found in many Baubotanik joints, living root bridges and naturally growing inosculations (as well as tree forks). Given the common growth ring forms around the entire inosculation (Millner 1932), this zone is likely to occur regardless of the inosculation type—crossed (as in this study) or parallel trunks (Ludwig 2012), or knots (as in the living root bridges) (Ludwig et al. 2019). Whilst this provides a broad scope for the present research, the diversity of forms makes it difficult to run studies like the present one, comparing across trees. Future studies should aim to make direct comparisons with the present results. This study does not differentiate between the pre-existing independent trees and the common growth that forms the interwoven zone because the *S. alba* saplings that the studied pairs originated from were so small that their mechanical effects were considered negligible. Models of inosculations with little common growth in comparison with pre-existing growth should incorporate this (Wang et al. 2021). Such a model would require documentation of the trees before inosculation. Given the importance of even a basic geometric characterisation, this documentation is also essential for predictive structural analysis. These should be aggregated with growth models and pruning plans.

Conclusion

This study shows that models of elastic behaviour in inosculations benefit from a combination of moderate geometric precision and a structural model that reflects local optimisations, such as the tension zone adaptation proposed bySlater et al. (2014). Drawing on the optimisations of naturally growing tree forks subject to similar physiological and mechanical pressures has yielded a fruitful model of inosculation mechanics. Finite element analysis of point cloud-derived meshes has yielded a method for analysing existing and predicted inosculations—an essential part of the iterative process of designing living architecture. If practitioners can capture and model the basic form of tree elements and joints, major improvements in structural models can be realised. Future studies should replicate the present models in new settings, investigating different species and inosculation forms. Deeper research into the failure modes of inosculations would give designers key insight into their practical use in structural engineering.

Author contribution statement WM, FL and AD: contributed to the study conception and design and the experimental setup. WM: carried out the experimental data collection. WM and HIE: created the finite element meshes and models. WM: did the post-processing and comparisons. FL and PD: provided critical feedback. The manuscript was written predominantly by WM with contributions from all authors.

Declarations

Conflict of interest The authors have no relevant financial or non-financial interests to disclose.

Open Access This article is licensed under a Creative Commons Attribution 4.0 International License, which permits use, sharing, adaptation, distribution and reproduction in any medium or format, as long as you give appropriate credit to the original author(s) and the source, provide a link to the Creative Commons licence, and indicate if changes were made. The images or other third party material in this article are included in the article's Creative Commons licence, unless indicated otherwise in a credit line to the material. If material is not included in the article's Creative Commons licence and your intended use is not permitted by statutory regulation or exceeds the permitted use, you will need to obtain permission directly from the copyright holder. To view a copy of this licence, visit http://creativecommons.org/licenses/by/4.0/.

References

Aliaga A (2017) "Casas vivas" de árboles, el maravilloso lugar en Punta de Agua. Argentina: Sitio Andino. https://www.sitioandino.com.ar/n/251521-casas-vivas-de-arboles-el-maravilloso-lugar-en-punta-de-agua/. Accessed 27 May 2022

Ansys (2022a) Ansys Mechanical Finite Element Analysis (FEA) Software for Structural Engineering. Canonsburg, Pennsylvania: Ansys. https://www.ansys.com/products/structures/ansys-mechanical. Accessed 25 May 2022

Ansys (2022b) Ansys SpaceClaim 3D Modelling Software. Canonsburg, Pennsylvania. https://www.ansys.com/products/3d-design/ansys-spaceclaim. Accessed 25 May 2022

Argus-Electronic (2016) PiCUS TreeQinetic. https://www.argus-electronic.de/en/tree-inspection/products/picus-treeqinetic. Accessed 19 May 2022

Beismann H, Wilhelmi H, Baillères H, Spatz H-C, Bogenrieder A, Speck T (2000) Brittleness of twig bases in the genus Salix: fracture mechanics and ecological relevance. J Exp Bot 51:617–633

Bowles JE (1988) Foundation analysis and design.

Burcham D (2020) The effect of pruning treatments on the vibration properties and wind-induced bending moments of Senegal mahogany (*Khaya senegalensis*) and rain tree (*Samanea saman*) in Singapore. University of Massachusetts Amherst

Burgert I, Jungnikl K (2004) Adaptive growth of gymnosperm branches-ultrastructural and micromechanical examinations. J Plant Growth Regul 23:76–82

Capuana M (2020) A review of the performance of woody and herbaceous ornamental plants for phytoremediation in urban areas. iFor Biogeosci For 13:139

Cignoni P (2018) Meshlab Homepage. http://www.meshlab.net/. Accessed 18 Sept 2018

Davies NT, Altaner CM, Apiolaza LA (2016) Elastic constants of green Pinus radiata wood. NZ J For Sci 46:1–6

Detter A, Rust S, Rust C, Maybaum G (2013) Determining strength limits for standing tree stems from bending tests. Proceedings of the 18th International Nondestructive Testing and Evaluation of Wood Symposium, Madison, WI, USA, p 24–27

Dounar S, Iakimovitch A, Mishchanka K, Jakubowski A, Chybowski L (2020) FEA simulation of the biomechanical structure overload in the university campus planting. Appl Bionics Biomech

Farrell RW (2003) Structural features related to tree crotch strength. Virginia Tech

Gilman EF (2003) Branch-to-stem diameter ratio affects strength of attachment. J Arboric 29:291–294

Girardeau-Montaut D (2011) Cloudcompare-open source project. OpenSource Proj 2.11.3 ed

Graham B, Bormann F (1966) Natural root grafts. Bot Rev 32:255–292

Harrison RDC, Chong KY, Pham NM, Yee ATK, Yeo CK, Tan HTW, Rasplus JY (2017) Pollination of Ficus elastica: India rubber re-establishes sexual reproduction in Singapore. Sci Rep 7:11616

Haushahn T, Speck T, Masselter T (2014) Branching morphology of decapitated arborescent monocotyledons with secondary growth. Am J Bot 101:754–763

Höpfl L, Sunguroğlu Hensel D, Hensel M, Ludwig F (2021) Initiating research into adapting rural hedging techniques, hedge types, and hedgerow networks as novel urban green systems. Land 10:529

Hui L, Jim CY, Zhang H (2020) Allometry of urban trees in subtropical Hong Kong and effects of habitat types. Landsc Ecol 35:1–18

Jackson T, Shenkin A, Wellpott A, Calders K, Origo N, Disney M, Burt A, Raumonen P, Gardiner B, Herold M (2019) Finite element analysis of trees in the wind based on terrestrial laser scanning data. Agric for Meteorol 265:137–144

Jungnikl K, Goebbels J, Burgert I, Fratzl P (2009) The role of material properties for the mechanical adaptation at branch junctions. Trees 23:605–610

Kane B (2007) Branch Strength of Bradford Pear (Pyrus calleryana var. Bradford'). Arboric Urban For 33**:**283

Kersten TP, Mechelke K, Lindstaedt M, Sternberg H (2009) Methods for geometric accuracy investigations of terrestrial laser scanning systems.

Kretschmann D (2010) Mechanical properties of wood. Wood handbook: wood as an engineering material: chapter 5. Centennial ed. General technical report FPL; GTR-190. Madison, WI: US Dept. of Agriculture, Forest Service, Forest Products Laboratory, 2010: p 5.1–5.46, 190**,** 5.1–5.46

Leclercq A (1997) Wood quality of white willow. BASE

Lichtenegger H, Reiterer A, Stanzl-Tschegg S, Fratzl P (1999) Variation of cellulose microfibril angles in softwoods and hardwoods—a possible strategy of mechanical optimization. J Struct Biol 128:257–269

Lievestro T (2020) Living trees as structural elements for vertical forest engineering.

Linaraki D, Watson J, Rousso B (2021) Growing Living Bridges in Mumbai. Responsive Cities, 2021 Barcelona. Barcelona: IAAC, p 34-47

Liu F, Zhang H, Jiang F, Wang X, Guan C (2019) Variations in orthotropic elastic constants of green Chinese larch from pith to sapwood. Forests 10:456

Ludwig F (2012) Botanische Grundlagen der Baubotanik und deren Anwendung im Entwurf. Doktorarbeit (PHD), Stuttgart

Ludwig F (2016) Baubotanik: Designing with Living Material. In: Löschke SK (eds) Materiality and Architecture. Routledge

Ludwig F, Middleton W, Gallenmüller F, Rogers P, Speck T (2019) Living bridges using aerial roots of ficus elastica–an interdisciplinary perspective. Sci Rep 9:1–11

Ludwig FM, Wilfrid Vees UTE (2019) Baubotanik: Living Wood and Organic Joints. In: Hudert MP, Sven (eds) Rethinking Wood. Birkhäuser, Basel, Switzerland

Margaretha E (2013) Growing Structure: Kagome Sandpit in Vienna. Munich: Detail. https://www.detail.de/en/de_en/growing-structure-kagome-sandpit-in-vienna-16526. Accessed 27 May 2022

Mattheck C, Bethge K (1998) The Structural Optimization of Trees. Naturwissenschaften 85:1–10

Matweb (2022) European Willow Wood Material Property Darta. matweb.com: matweb.com. https://www.matweb.com/search/DataSheet.aspx?MatGUID=d0fce8e05e2d41ae9676addf6aeb3e6c. Accessed 19 May 2022

Mcbride JR (2017) The world's urban forests. Springer

Meier E (2022) White Willow. wood-database.com: wood-database. com. https://www.wood-database.com/white-willow/. Accessed 19 May 2022

Middleton W, Habibi A, Shankar S, Ludwig F (2020) Characterizing regenerative aspects of living root bridges. Sustainability 12:3267

Middleton W, Shu Q, Ludwig F (2019) Photogrammetry as a tool for living architecture. Int Arch Photogramm Remote Sens Spat Inf Sci 42:195–201

Middleton W, Shu Q, Ludwig F (2022) Representing living architecture through skeleton reconstruction from point clouds. Sci Rep 12:1–13

Millner EM (1932) Natural grafting in hedera helix. New Phytol 31:2–25

Moravčík Ľ, Vincúr R, Rózová Z (2021) Analysis of the static behavior of a single tree on a finite element model. Plants 10:1284

Müller U, Gindl W, Jeronimidis G (2006) Biomechanics of a branch–stem junction in softwood. Trees 20:643–648

Niklas KJ, Spatz HC (2010) Worldwide correlations of mechanical properties and green wood density. Am J Bot 97:1587–1594

Ozyhar T, Hering S, Niemz P (2013) Moisture-dependent orthotropic tension-compression asymmetry of wood. Holzforschung 67:395–404

Pfisterer JA, Spatz HC (2008) Untersuchungen zu drei unterschiedlichen Achselholztypen: Anatomische und biomechanische Eigenschaften von Achselholz. AFZ-DerWald. pp 632–35

Riegl (2010) LMS-Z420i Data Sheet. Riegl Laser Measurement Systems. http://www.riegl.com/uploads/tx_pxpriegldownloads/10_DataSheet_Z420i_03-05-2010.pdf . Accessed 19 May 2022

Shigo AL (1985) How tree branches are attached to trunks. Can J Bot 63:1391–1401

Shu Q, Middleton W, Ludwig F (2021) Teaching computational approaches in Baubotanik. Responsive Cities 2021: design with nature, Barcelona. IAAC, pp 212–221

Slater D (2018a) The association between natural braces and the development of bark-included junctions in trees. Arboric J 40:16–38

Slater D (2018b) Natural bracing in trees: management recommendations. Arboric J 40:106–133

Slater D (2021) The mechanical effects of bulges developed around bark-included branch junctions of hazel (*Corylus avellana* L.) and other trees. Trees 35:513–526

Slater D, Bradley RS, Withers PJ, Roland Ennos A (2014) The anatomy and grain pattern in forks of hazel (Corylus avellana L.) and other tree species. Trees 28:1437–1448

Slater D, Ennos AR (2013) Determining the mechanical properties of hazel forks by testing their component parts. Trees 27:1515–1524

Smith S (2013) Willow bridge officially opened. Cambridge, UK: Smith and Wallwork Engineers. https://www.smithandwallwork.com/whats-new/willow-bridge-officially-opened/. Accessed 27 May 2022

Van Casteren A, Sellers W, Thorpe S, Coward S, Crompton R, Ennos A (2012) Why don't branches snap? The mechanics of bending failure in three temperate angiosperm trees. Trees 26:789–797

Vojáčková B, Tippner J, Horáček P, Praus L, Sebera V, Brabec M (2019) Numerical Analysis of Branch Mechanical Response to Loading. Arboric Urban For 45

Wang X, Gard W, de Vries N, van de Kuilen J-W (2021) Anatomical and Mechanical Features of Self-Growing Connections in Plants. Available at SSRN 3970513

Wessolly L, ERB M (2014) Handbuch der Baumstatik und Baumkontrolle, Patzer.

Yang M, Défossez P, Danjon F, Dupont S, Fourcaud T (2017) Which root architectural elements contribute the best to anchorage of Pinus species? Insights from in silico experiments. Plant Soil 411:275–291

Yang M, Défossez P, Danjon F, Fourcaud T (2014) Tree stability under wind: simulating uprooting with root breakage using a finite element method. Ann Bot 114:695–709